Available online at www.sciencedirect.com
ScienceDirect
Trans. Nonferrous Met. Soc. China 32(2022) 262−272
Transactions of Nonferrous Metals Society of China
www.tnmsc.cn

Enhancing storage performance of P2-type $Na_{2/3}Fe_{1/2}Mn_{1/2}O_2$ cathode materials by Al_2O_3 coating

Yi-jiao CHANG, Guang-hui XIE, Yong-mao ZHOU, Jie-xi WANG, Zhi-xing WANG, Hua-jun GUO, Bian-zheng YOU, Guo-chun YAN

School of Metallurgy and Environment, Central South University, Changsha 410083, China

Received 15 February 2021; accepted 26 September 2021

Abstract: The P2-type $Na_{2/3}Fe_{1/2}Mn_{1/2}O_2$ materials were synthesized by an ultrasonic spray pyrolysis followed by solid-state sintering method. The structures, morphologies and electrochemical performances of $Na_{2/3}Fe_{1/2}Mn_{1/2}O_2$ materials were characterized thoroughly by means of X-ray diffractometer, scanning electron microscope and electrochemical charge/discharge instruments. Moreover, a thin layer of Al_2O_3, which was formed on the surface of $Na_{2/3}Fe_{1/2}Mn_{1/2}O_2$, can enhance the storage performance by preventing the formation of $Na_2CO_3·H_2O$, which is believed to enhance the electrochemical performances of $Na_{2/3}Fe_{1/2}Mn_{1/2}O_2$ materials. This facile surface modification method may pave a way to synthesize advanced cathode materials for sodium-ion batteries.

Key words: Al_2O_3 coating; air-stability; spray pyrolysis; sodium-ion batteries; iron−manganese oxide

1 Introduction

Although the research on sodium-ion batteries and lithium-ion batteries almost simultaneously began in 1970s, sodium-ion batteries gradually faded out of sight due to the rapid growth and improved performance of lithium-ion batteries. After being commercially applied by Sony Company in 1990s, lithium-ion batteries are widely used in portable electronic devices and electric vehicles due to their high energy density and operating voltage [1−7]. In recent years, we have witnessed the demand for renewable large-scale electrochemical energy storage systems, which makes the sodium-ion batteries regain attention [8−10]. Because of the widespread distribution of sodium resources and low cost, sodium-ion batteries have become an advantageous candidate to replace lithium-ion batteries in large-scale electrochemical energy storage systems [11,12]. In addition, sodium ions have larger radius (1.02 Å) when compared with lithium ions (0.76 Å) [13], thus the problem of mixing alkali metal ions and transition metal ions can be effectively avoided to achieve a better long-cycling performance [14−17].

As far as we know, research on cathodes for sodium-ion batteries is mainly focused on sodium layered oxides and polyanionic compounds (e.g., $Na_3V_2(PO_4)_2F_3$) [18,19]. Layered transition metal oxide material, which can be divided into P2 and O3 phases (P represents prismatic, and O represents octahedral) according to the coordination polyhedrons where sodium ions are located and different stacking ways of transition metal oxide layers, is considered as the most promising candidate due to its high theoretical specific capacities [20−23]. In Na_xMeO_2 (Me=Ni [24], Co [25,26], Mn [27−29], Fe [30,31], Cr [32] etc. and their combinations), x is usually between 0.6 and 0.7 within P2 phase structure, and sodium ions are in prismatic coordination that is relatively

Corresponding author: Guo-chun YAN, Tel: +86-15273163234, E-mail: happyygc@csu.edu.cn
DOI: 10.1016/S1003-6326(22)65792-3

stable. Nevertheless, the layered transition metal oxide cathode materials show poor air stability. After contacting with moisture and carbon dioxide, side reactions will happen, which deteriorate the electrochemical performance of the material [33,34]. The poor air-storage performance substantially increases the cost of material preparation, storage and transportation, which limits the commercial application of layered transition metal oxide cathode materials. To solve this problem, some modified strategies have been adopted. LI et al [35] entirely substituted Ni with Cu and introduced Fe into the $Na_{2/3}Ni_{1/3}Mn_{2/3}O_2$ by a solid-state method, ultimately succeeded in synthesizing air-stable P2-$Na_{7/9}Cu_{2/9}Fe_{1/9}Mn_{2/3}O_2$ materials. A combined structural modulation via Cu/Ti co-doping was adopted, and the results showed impactful effect on enhancing the air stability of O3-phase $NaNi_{0.5}Mn_{0.5}O_2$ cathodes [36]. Additionally, a novel ethanol washing way was used to remove the residual sodium salts on the surface of $NaNi_{0.5}Mn_{0.5}O_2$ materials, which improved air stability [37].

As P2-type iron−manganese oxide materials like $Na_{2/3}Fe_{1/2}Mn_{1/2}O_2$ show higher specific capacity, we synthesized P2-type $Na_{2/3}Fe_{1/2}Mn_{1/2}O_2$ material via an ultrasonic spray pyrolysis followed by solid-state sintering method, and studied the transformation of materials under inert and air conditions (a relative humidity of ~55%). P2-$Na_{2/3}Fe_{1/2}Mn_{1/2}O_2$ delivers a reversible initial discharge capacity of 156.6 mA·h/g at a current rate of 0.1*C* (1*C*=260 mA/g). As the materials are unstable in air, Al_2O_3 coating layer was introduced onto the surface of $Na_{2/3}Fe_{1/2}Mn_{1/2}O_2$ material, which can effectively improve the electrochemical performance of the materials after being stored in air.

2 Experimental

2.1 Materials synthesis

The $Na_{2/3}Fe_{1/2}Mn_{1/2}O_2$ (hereafter denoted as NFMO) samples were prepared by an ultrasonic spray pyrolysis followed by solid-state sintering method. The precursor solution was prepared by dissolving ferric(III) nitrate nonahydrate and manganese(II) nitrate tetrahydrate with deionized water under stirring, in which the molar ratio of metal component (Fe to Mn) was 1:1. The mixed solution was atomized by ultrasonic atomizer to form small droplets. With the carrier gas (high purity O_2) at a flow rate of 5 L/min, the droplets were loaded into the spray pyrolysis furnace and pyrolyzed at 800 °C to obtain the precursor of ferric and manganese oxide ($Fe_{1/2}Mn_{1/2}O_2$) with waxberry-like spherical morphology (see Fig. 1(a)) and Fe, Mn, and O elements distribute uniformly (see Fig. 1(b)). After measuring the element contents of Fe and Mn in $Fe_{1/2}Mn_{1/2}O_2$ precursor by inductive coupled plasma (ICP) emission spectrometer (see Table 1), the precursors were mixed with the sodium source (Na_2O_2, 3 wt.% excess of sodium) in the glove box and were fully ground for 1 h to make the raw materials evenly mixed. Then, the mixed raw materials were sintered in a tubular furnace in the air atmosphere at a temperature of 900 °C for 9 h and the heating rate is 5 L/min. Afterwards, the products were naturally cooled down to about 200 °C, and the as-synthesized NFMO powders were quickly sealed and preserved to avoid the contact with water and CO_2 in air.

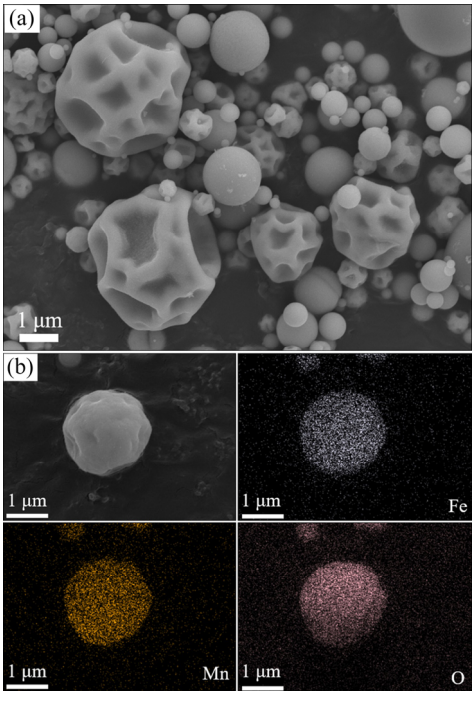

Fig. 1 SEM image (a) and EDS elemental mapping results (b) of $Fe_{1/2}Mn_{1/2}O_2$ precursor samples

Table 1 Metal contents of $Fe_{1/2}Mn_{1/2}O_2$ precursor measured by ICP

Element	Content/at.%	Content/wt.%
Fe	17.85	33.04
Mn	18.15	33.11

To prepare the Al_2O_3-coated NFMO material, 0.3678 g $Al(NO_3)_3·9H_2O$ was dissolved in 200 mL deionized water, and was stirred at room temperature for 1 h. 5 g NFMO material was dispersed in the solution and stirred for 2 h to obtain evenly dispersed suspension. The suspension was transferred to a water bath at 80 °C for heating and stirring simultaneously. After the solution was completely steamed and dried, the powder material was taken out and dried in a blast drying oven at 80 °C. After that, the samples were heat-treated in a tubular furnace at 500 °C to decompose $Al(NO_3)_3$ completely. Eventually, Al_2O_3 was coated on the surface of NFMO material, which was labeled as NFMO-Al_2O_3. The chemical composition of the NFMO-Al_2O_3 materials was measured via ICP (see Table 2).

Table 2 Contents of NFMO-Al_2O_3 materials measured by ICP

Element	Content/at.%	Content/wt.%
Na	18.26	14.862
Fe	13.76	27.164
Mn	13.46	26.507
Al	0.73	0.918

2.2 Materials characterization

The chemical composition of all the samples was measured via ICP (Thermo Fisher Scientific ICAP 7400 Radial). 30 mg of the precursor material prepared was dissolved in hydrochloric acid with a concentration of 1 mol/L and diluted to a constant volume of 1 L. A small amount of dilute solution with constant volume was used for ICP analysis to obtain the concentration of metal ions in the solution. The crystal phases of the obtained products were identified by powder X-ray diffraction in a 2θ range of 10°−60° (XRD, Rigaku TTRⅢ) with Cu K_α radiation (λ=1.54184 Å). Scanning electron microscope (SEM, JEOL JSM−7900F) was used to analyze the morphology of the samples. Energy dispersive X-ray spectroscopy (EDS) elemental mapping was collected on a JEOL JSM−7900F instrument. Transmission electron microscopy (TEM, FEI Tecnai G2 F20 S-TWIN TMP) images and high-resolution TEM images were recorded to analyze the Al_2O_3 coating layer. Fourier transform infrared spectroscope (FTIR, Nicolet AVATAR 360) was used to analyze the functional groups on the surface of materials.

2.3 Electrochemical measurements

The electrochemical measurements were conducted using coin-type cells (CR 2025). The active material, conductive carbon (Keqin black) and polyvinylidene fluoride (PVDF) binder with the mass ratio of 8:1:1 were fully ground in an agate mortar for 15 min. Then, appropriate amount of N-methyl-2-pyrrolidone (NMP) was added and continuously ground until it became slurry with moderate viscosity. The gained slurry was coated on Al foil and dried at 120 °C for 6 h. The fabricated cathodes were cut into 14 mm circular electrodes, which were dried in an vacuum oven (60 °C) together with the prepared glass fiber separator (Whatman GF/A, 18 mm), nickel mesh, anode and cathode battery shell for 6 h. 1 mol/L $NaClO_4$ in propylene carbonate with 5% fluoroethylene carbonate (Kishida chemical) and sodium foil with a diameter of 16 mm were used as the electrolyte and the anode, respectively. Coin-type cells (CR 2025) were assembled in a dry argon-filled glove box. The reversible specific capacity and cycle stability were measured on a NEWARE charge−discharge tester at a voltage of 1.5−4.0 V (vs Na/Na^+).

3 Results and discussion

3.1 Structure and morphology of P2-type NFMO

As evidenced by the XRD results (see Fig. 2), the pure NFMO was synthesized by an ultrasonic spray pyrolysis followed by solid-state sintering method, which shows a plate-like morphology (Fig. 3).

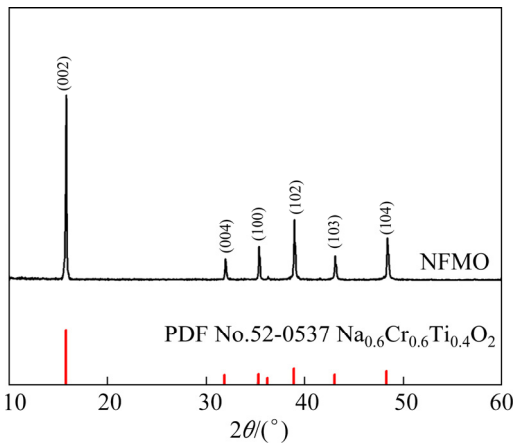

Fig. 2 XRD pattern of P2-type NFMO samples

3.2 Storage performance of P2-type NFMO

As depicted in Fig. 4(a), NaO_6 prims share faces or edges with MeO_6 octahedra in the structure of NFMO, in which sodium ions have two kinds of occupied sites, namely Na_f and Na_e. Due to the long distance between sodium ions and transition metal

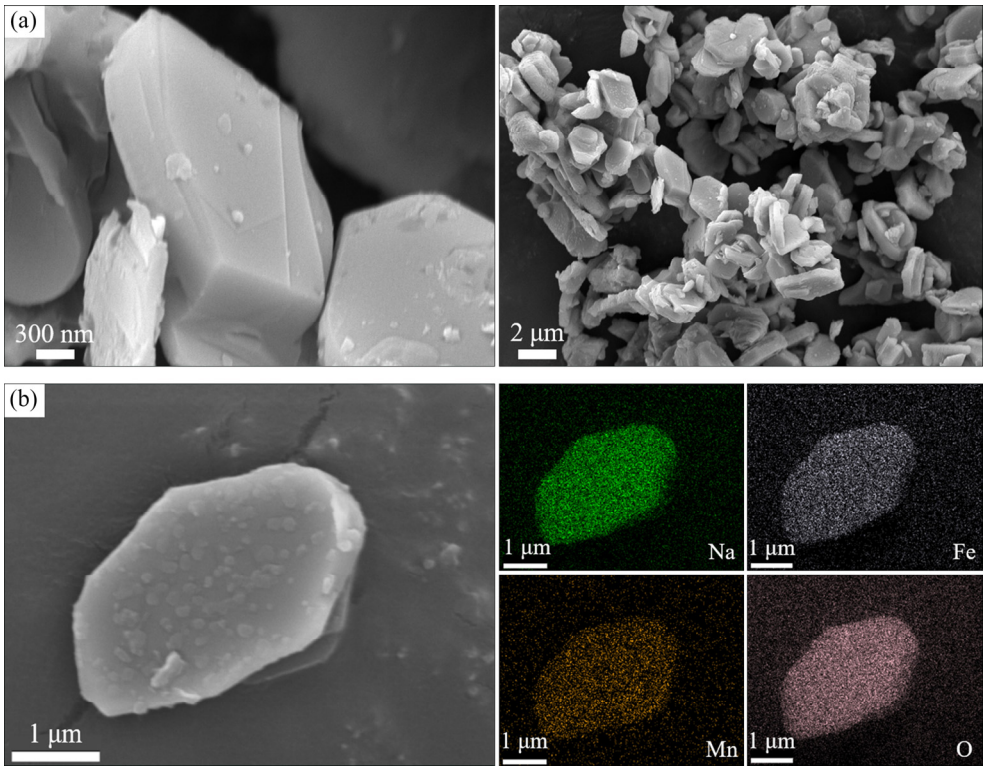

Fig. 3 SEM images (a) and EDS elemental mapping results (b) of P2-type NFMO samples

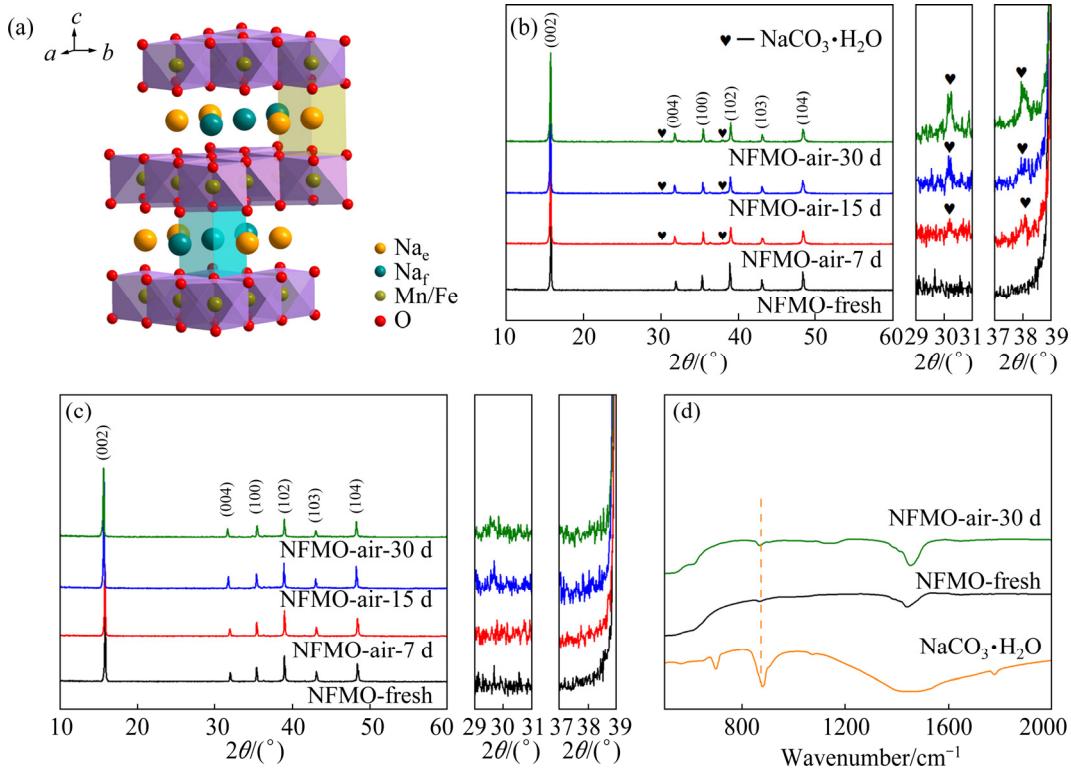

Fig. 4 Schematic diagram of crystal structure for P2-type NFMO materials (a), XRD patterns of NFMO materials before and after storage in air (b) and argon (c), and FTIR spectra of $Na_2CO_3·H_2O$, fresh NFMO and NFMO stored in air for 30 d

ions, which can reduce the cation repulsion, the Na_e site is more stable than Na_f site. Therefore, a part of sodium ions tend to diffuse out of the crystal lattice and react with moisture and carbon dioxide. We carried out an investigation on air-storage properties of the P2-type NFMO material. The as-synthesized NFMO samples were stored in inert (argon) and ambient air (relative humidity of ~55%) for 7, 15 and 30 d, respectively. As shown in Fig. 4(b), the pristine NFMO has an ideal P2 structure. After being exposed to air for 7 d, the XRD patterns show impurity peaks at 2θ of 30.18° and 37.99° (enlarged XRD patterns of NFMO-exposed series in Fig. 4(b)), which can be indexed to $Na_2CO_3·H_2O$. After extending the storage time to 15 and 30 d, the peak intensity increased obviously. Figure 4(c) shows that NFMO-fresh material was stored in inert atmosphere and the diffraction peaks of argon-storage samples were completely consistent with those of the fresh material. Even the storage time was extended to 15 and 30 d, the intensity of the diffraction peak was almost unchanged, which indicates that the NFMO material does not generate impurities when stored in the inert atmosphere, and the crystalline structure of the material is well maintained. In order to confirm the impurities on the air-exposed NFMO samples, we employed FTIR to characterize the as-synthesized NFMO powders, air-exposed NFMO powders and $Na_2CO_3·H_2O$ (Fig. 4(d)). Within the wavenumber range from 500 to 2000 cm^{-1}, the characteristic peak of $Na_2CO_3·H_2O$ at 874.4 cm^{-1} is observed in NFMO-air-30 d sample, which corresponds to CO_3^{2-} vibrations. Compared with the freshly prepared samples, the characteristic peak becomes intense after air exposure, suggesting that the exposing process is accompanied by the generation of $Na_2CO_3·H_2O$. The proposed reactions are given below:

$$2Na_{2/3}Fe_{1/2}Mn_{1/2}O_2+xCO_2+1/2xO_2\rightarrow xNa_2CO_3+2Na_{2/3-x}Fe_{1/2}Mn_{1/2}O_2 \quad (1)$$

$$Na_2CO_3+H_2O\rightarrow Na_2CO_3·H_2O \quad (2)$$

The galvanostatic charge−discharge (GCD) curves of NFMO pristine materials in ambient air with different storage time cycled at 0.1C and 1.5−4.0 V are presented in Figs. 5(a) and (b). The initial charge and discharge specific capacities are

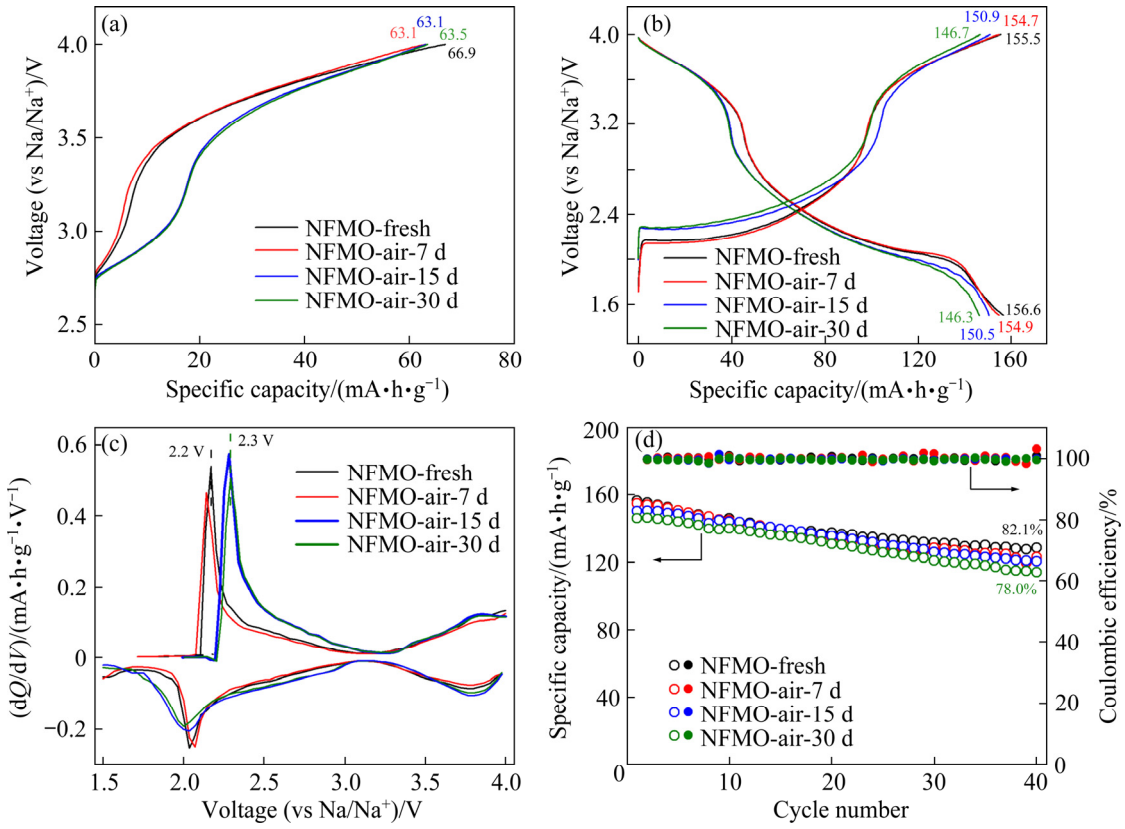

Fig. 5 Electrochemical properties of NFMO samples before and after storage in air: (a) Initial charge process at 0.1C; (b) Discharge process in the first cycle and charge process in the second cycle at 0.1C; (c) dQ/dV vs voltage curves in the second cycle; (d) Electrochemical cycling performance at 0.1C

66.9 and 156.6 mA·h/g of the freshly prepared NFMO materials, respectively (see Fig. 6(a)), and they decline to 63.5 and 146.3 mA·h/g after 30 d of air exposure (Figs. 5(a) and (b)). The initial charge and discharge specific capacities decrease notably with the extension of the exposure time, owing to the spontaneous movement of sodium ions from the bulk structure to the particle surface due to the side reactions with H_2O and CO_2. The resultant residual sodium compounds (such as Na_2CO_3 and their hydrates) contribute to sodium depletion, increasing polarization and capacity decay. Obviously, the deterioration exhibits a positive correlation with the extended air-storage time. As shown in Figs. 5(c) and 6(b), the NFMO-fresh materials show smaller difference between the anodic and cathodic peak (ΔV) than the air-exposed NFMO materials, indicating that the side reactions brought higher polarization during charge−discharge process. The derivate plot of GCD curves is consistent with the results in Figs. 5(a) and (b). After being exposed in air for a period of time, the electrochemically insulated $Na_2CO_3{\cdot}H_2O$ emerges on the surface of the NFMO particles, resulting in poor sodium-ion diffusion kinetics and aggravated polarization. Figure 5(d) exhibits the cycle performance of NFMO-fresh and NFMO-air samples at 0.1C. Freshly prepared NFMO materials deliver a discharge specific capacity of 156.6 mA·h/g at the first cycle, the capacity retention reaches nearly 82.1% after 40 cycles (see Fig. 6(c)). However, the capacity retention of materials decreases to 78.0% after being exposed in air for 30 d. The autogenous diffusion of sodium ions from the bulk and the consuming reaction between NFMO cathodes and air cause the depletion of sodium ions and the collapse of the crystal structure, which will have an adverse effect on the cycle performance of the electrode material.

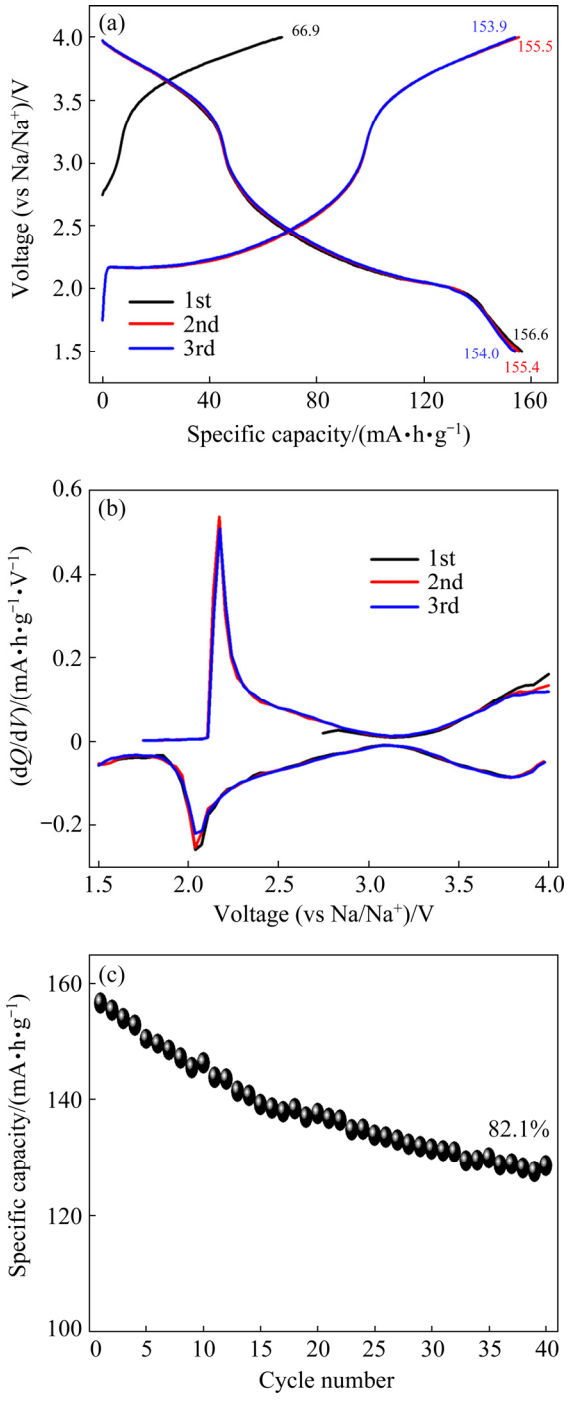

Fig. 6 Electrochemical properties of P2-type NFMO material: (a) Galvanostatic charge−discharge curves of the first three cycles at 1.5−4.0 V and 0.1C; (b) dQ/dV vs voltage curves for the first, second, and third cycles; (c) Electrochemical cycling performance at 0.1C

3.3 Storage performance of Al_2O_3-coated NFMO

As NFMO materials are easily deteriorated in ambient atmosphere, we modified the surface of NFMO particles with an inert Al_2O_3 to improve the air-storage performance of the materials. Surface energy dispersive spectrometry (EDS, Fig. 7(a)), transmission electron microscopy (TEM, Fig. 7(b)) image and high-resolution transmission electron microscopy (HRTEM, Fig. 7(c)) image confirm the existence of Al_2O_3 coating layer. It is notable that a small amount of Al element is detected on the surface of the NFMO particles, as presented in Fig. 7(a), meanwhile Na, Fe, Mn and O elements of the particles are evenly distributed. The TEM image shows that the Al_2O_3 modifying layer is inhomogeneously coated onto the surface of NFMO

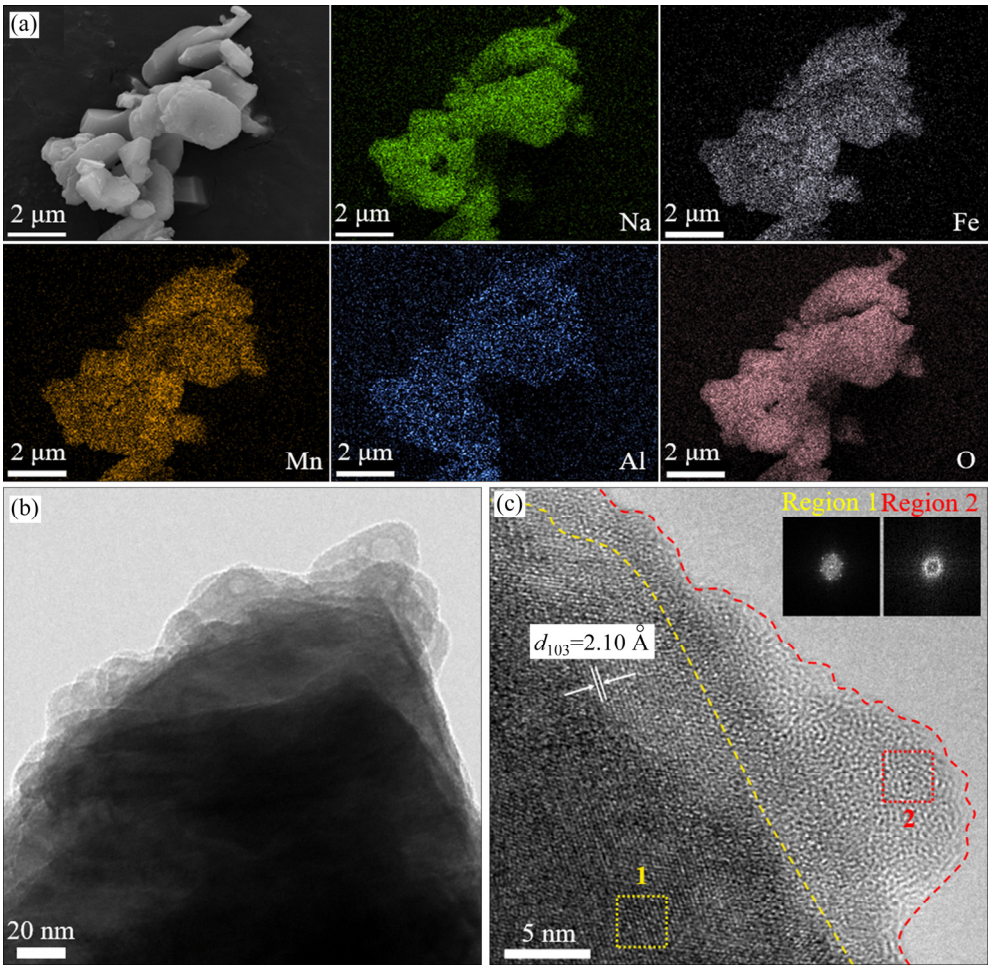

Fig. 7 EDS mapping results (a), TEM image (b) and HRTEM image and corresponding FFT images of Regions 1 and 2 (c) of NFMO-Al_2O_3 samples

materials, and the thickness of which ranges from ~2 to ~20 nm. Figure 7(c) shows the HRTEM image of Al_2O_3-coated NFMO materials. Two kinds of disparate crystal lattices occur from the bulk to the surface, the interplanar spacing value of 2.10 Å belongs to (103) plane of NFMO materials, and amorphous crystal lattices (Region 2) can be assigned to the Al_2O_3 coating layer. Fast Fourier transform (FFT) images of Regions 1 and 2 clearly distinguish the two distinct structures in the dotted yellow and red boxes, respectively.

To evaluate the effect of Al_2O_3 coating layer on the air-storage performance of the materials, the as-synthesized NFMO and NFMO-Al_2O_3 samples were exposed in air, simultaneously another equal amount of freshly prepared NFMO sample was stored in Ar-filled glovebox as a contrast. Concentrations of the residual sodium ions on the surfaces of NFMO and NFMO-Al_2O_3 materials under different storage conditions are shown in Fig. 8, which was determined through ICP analysis by immersing the exposed powder in deionized water for 12 h to dissolve residual sodium species (Na_2CO_3 and $Na_2CO_3·H_2O$). Even being stored in inert atmosphere, the residual sodium salt concentrations increased slightly with the extension of storage time (4.15, 5.01 and 5.86 mg/L at 7, 15 and 30 d, respectively), which may arise from the excess Na sources in solid-state sintering process. In addition, the concentration of residual sodium salts underwent an abrupt growth along with the air-storage time increasing (10.52, 17.22 and 21.91 mg/L at 7, 15 and 30 d, respectively). Furthermore, the concentration of residual sodium salts is much higher than that of the samples stored in inert atmosphere, ascribing to the deterioration of materials stored in air and the chemical reactions between air and materials producing soluble sodium

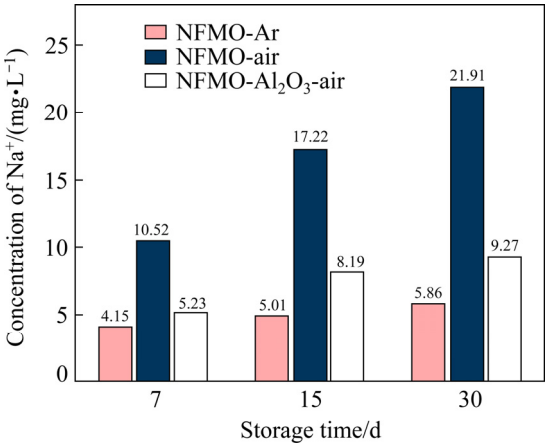

Fig. 8 Concentrations of residual sodium ions on NFMO surfaces after storage in air and argon, and NFMO-Al_2O_3 after storage in air

salts. Small quantities of sodium ions (5.23 mg/L) are detected in the NFMO-Al_2O_3 materials exposed to air for 7 d. This may originate from the excess sodium sources on the particle surfaces during the solid-state sintering process and weak reaction with air. With the extension of storage time, the concentration of sodium ions increased slightly (8.19 and 9.27 mg/L at 15 and 30 d, respectively). Compared with samples stored in argon atmosphere, the sodium ion concentration of Al_2O_3-coated materials is higher, ascribing to the unevenly coating and the intricate side reactions with air. However, we find that the concentration of the residual sodium species on the Al_2O_3-modified materials is obviously lower than that of the air-exposed NFMO materials. Even storage in air for 30 d, the concentration of sodium ions in the filtrate of NFMO-Al_2O_3 materials is only 9.27 mg/L, which is far less than the concentration of NFMO-air-30 d materials (21.91 mg/L). This confirms that the Al_2O_3 coating layer on the surface of NFMO particles inhibits the deterioration of the materials when stored in air, which isolates air and protects sodium ions from directly contacting with CO_2 and H_2O in air.

Figure 9(a) shows the XRD patterns of Al_2O_3-coated NFMO materials after being exposed in air for various time. All XRD peaks are well indexed to the ideal P2-type crystal structure (space group: *P*63/*mmc*). After 30 d of exposure, the position and intensity of diffraction peaks of the coated materials exhibit negligible change, which indicates that coated materials maintain original

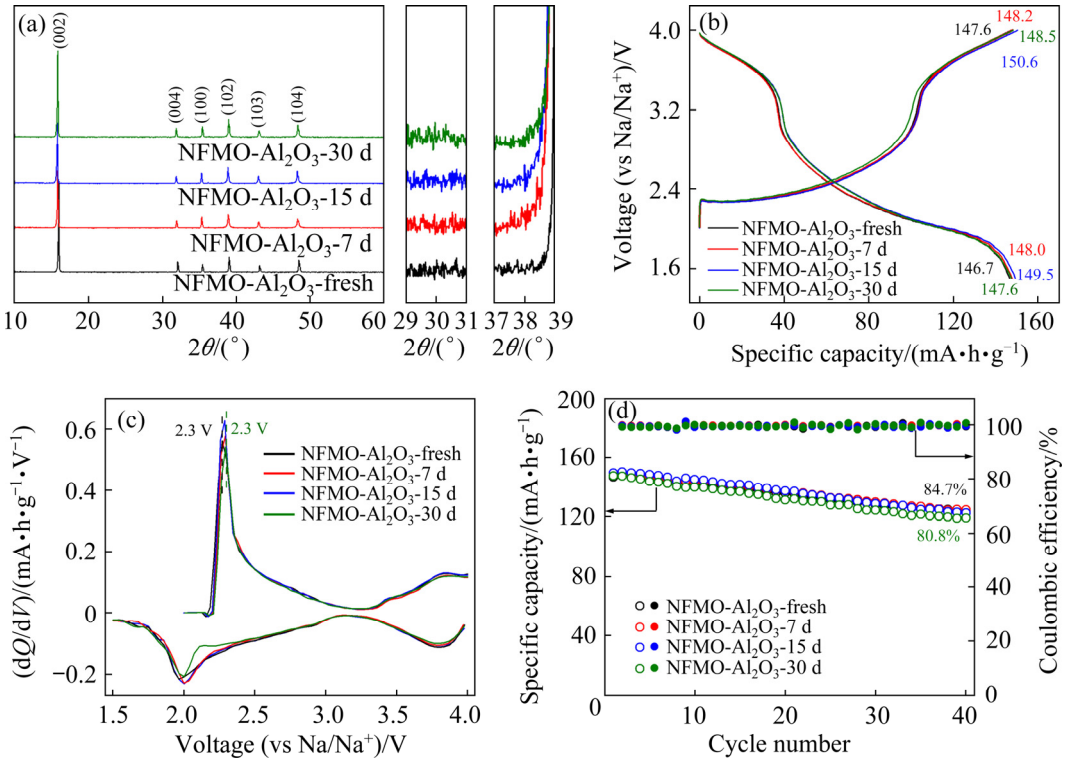

Fig. 9 XRD patterns and electrochemical results of NFMO-Al_2O_3 materials before and after storage in air: (a) XRD patterns; (b) Discharge process in the first cycle and charge process in the second cycle at voltage of 1.5−4.0 V and 0.1*C*; (c) d*Q*/d*V* vs voltage curves in the second cycle; (d) Electrochemical cycling performance at 0.1*C*

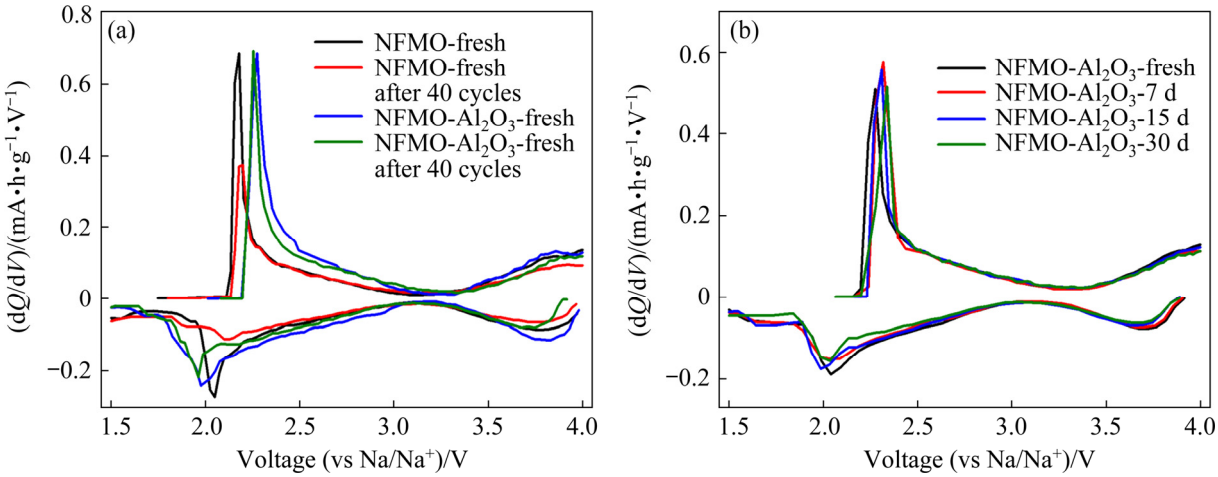

Fig. 10 dQ/dV vs voltage curves for NFMO-fresh and NFMO-Al_2O_3 samples before and after 40 cycles (a) and dQ/dV vs voltage for NFMO-Al_2O_3 samples at different storage time after 40 cycles (b)

crystal structure, and no impurities are formed during exposure. The galvanostatic charge−discharge (GCD) profiles of air-exposed Al_2O_3-coated NFMO materials are shown in Fig. 9(b). In comparison with the uncoated pristine materials, the coated pristine materials show discharge specific capacity of 146.7 mA·h/g in the first cycle. However, after 40 cycles, NFMO-Al_2O_3 materials exhibit higher capacity retention of 84.7% (Fig. 9(d)) as compared with that of NFMO-fresh materials (82.1%). Although parts of the specific capacities are sacrificed, the Al_2O_3 coating layer improves the cyclic stability of the materials. With the storage time extending to 30 d, the capacity retention of coated materials only decreases to 80.8% (Fig. 9(d)), which is higher than that of air-exposed NFMO pristine materials with the same storage time (78.0%, Fig. 5(d)). As shown in Fig. 9(c), Al_2O_3-coated NFMO materials exhibit negligible polarization with the extension of air-storage time compared with that of uncoated counterparts. Similarly, no obvious polarizations are observed in the GCD profiles. Compared with uncycled NFMO-Al_2O_3 samples, the NFMO-Al_2O_3 materials after 40 cycles exhibit tiny polarization and capacity loss, while the NFMO-fresh materials exhibit huge capacity attenuation after cycling. Even exposed in air for 30 d, the changes of NFMO-Al_2O_3 samples are also minimal (see Fig. 10). The above results confirmed that Al_2O_3 coating layer can effectively improve the air-storage performance of NFMO materials, thus enhancing the cycle stability of NFMO materials after being exposed in air.

4 Conclusions

(1) P2-type $Na_{2/3}Fe_{1/2}Mn_{1/2}O_2$ materials were prepared by an ultrasonic spray pyrolysis followed by solid-state sintering method.

(2) After being exposed for a period of time in air, a small part of sodium ions in the $Na_{2/3}Fe_{1/2}Mn_{1/2}O_2$ spontaneously diffuse out of the crystal lattice to the surface, reacting with the carbon dioxide and moisture, thus generating Na_2CO_3 and $Na_2CO_3·H_2O$ on the surface of particles.

(3) The instability of $Na_{2/3}Fe_{1/2}Mn_{1/2}O_2$ against air can be optimized by modifying its surface with Al_2O_3 coating layer. The enhanced cyclic stability and reduced residual sodium ions concentration confirm that Al_2O_3 coating layer can protect $Na_{2/3}Fe_{1/2}Mn_{1/2}O_2$ from contacting with air and suppress the adverse side reactions when experiencing air exposure. This strategy can also be applied to other air-sensitive materials.

Acknowledgments

This work is financially supported by the Natural Science Foundation of Hunan Province, China (No. 2020JJ5755), the National Natural Science Foundation of China (Nos. 51804344, 51704332, 51874360), and the Innovation and Entrepreneurship Project of Hunan Province, China (No. 2018GK5026).

References

[1] SLATER M D, KIM D, LEE E, JOHNSON C S. Sodium-ion batteries [J]. Advanced Functional Materials, 2013, 23(8): 947−958.

[2] PALOMARES V, SERRAS P, VILLALUENGA I, HUESO K B, CARRETERO-GONZÁLEZ J, ROJO T. Na-ion batteries, recent advances and present challenges to become low cost energy storage systems [J]. Energy & Environmental Science, 2012, 5(3): 5884−5901.

[3] MARIYAPPAN S, WANG Qing, TARASCON J M. Will sodium layered oxides ever be competitive for sodium ion battery applications? [J]. Journal of the Electrochemical Society, 2018, 165(16): A3714−A3722.

[4] LIU Qian-nan, HU Zhe, CHEN Ming-zhe, ZOU Chao, JIN Hui-le, WANG Shun, CHOU Shu-lei, DOU Shi-xue. Recent progress of layered transition metal oxide cathodes for sodium-ion batteries [J]. Small, 2019, 15(32): e1805381.

[5] LI Ling-jun, XIA Ling-feng, YANG Hui-ping, ZHAN Xue-hui, CHEN Jie, CHEN Zhao-yong, DUAN Jun-fei. Solid-state synthesis of lanthanum-based oxides Co-coated $LiNi_{0.5}Co_{0.2}Mn_{0.3}O_2$ for advanced lithium ion batteries [J]. Journal of Alloys and Compounds, 2020, 832: 154959.

[6] PAN Cheng-chi, YANG Ying-chang, HOU Hong-shuai, JING Ming-jun, ZHU Yi-rong, SONG Wei-xing, JI Xiao-bo. Effect of lithium content on electrochemical property of $Li_{1+x}(Mn_{0.6}Ni_{0.2}Co_{0.2})_{1-x}O_2$ ($0\leq x\leq 0.3$) composite cathode materials for rechargeable lithium-ion batteries [J]. Transactions of Nonferrous Metals Society of China, 2018, 28(1): 145−150.

[7] CHEN Qi-chao, YAN Guan-jie, LUO Li-ming, CHEN Fei, XIE Tang-feng, DAI Shi-can, YUAN Ming-liang. Enhanced cycling stability of Mg−F co-modified $LiNi_{0.6}Co_{0.2}Mn_{0.2-y}Mg_yO_{2-z}F_z$ for lithium-ion batteries [J]. Transactions of Nonferrous Metals Society of China, 2018, 28(7): 1397−1403.

[8] LI Yun-ming, LU Ya-xiang, ZHAO Cheng-long, HU Yong-sheng, TITIRICI M M, LI Hong, HUANG Xue-jie, CHEN Li-quan. Recent advances of electrode materials for low-cost sodium-ion batteries towards practical application for grid energy storage [J]. Energy Storage Materials, 2017, 7: 130−151.

[9] PAN Wei, PENG Wen-jie, YAN Guo-chun, GUO Hua-jun, WANG Zhi-xing, LI Xin-hai, GUI Wei-hua, WANG Jie-xi, CHEN Ning. Suppressing the voltage decay and enhancing the electrochemical performance of $Li_{1.2}Mn_{0.54}Co_{0.13}Ni_{0.13}O_2$ by multifunctional Nb_2O_5 coating [J]. Energy Technology, 2018, 6(11): 2139−2145.

[10] LU Shi-jie, LIU Yang, HE Zhen-jiang, LI Yun-jiao, ZHENG Jun-chao, MAO Jing, DAI Ke-hua. Synthesis and properties of single-crystal Ni-rich cathode materials in Li-ion batteries [J]. Transactions of Nonferrous Metals Society of China, 2021, 31(4): 1074−1086.

[11] CHEN Jun, ZOU Guo-qiang, DENG Wen-tao, HUANG Zhao-dong, GAO Xu, LIU Cheng, YIN Shou-yi, LIU Huan-qing, DENG Xing-lan, TIAN Ye, LI Jia-yang, WANG Chi-wei, WANG Di, WU Han-wen, YANG Li, HOU Hong-shuai, JI Xiao-bo. Pseudo-bonding and electric-field harmony for Li-rich Mn-based oxide cathode [J]. Advanced Functional Materials, 2020, 30(46): 2004302.

[12] LIU Zeng-sheng, LI Ling-jun, CHEN Jie, YANG Hui-ping, XIA Ling-feng, CHEN Jia-xin, DUAN Jun-fei, CHEN Zhao-yong. Effects of chelating agents on electrochemical properties of $Na_{0.9}Ni_{0.45}Mn_{0.55}O_2$ cathode materials [J]. Journal of Alloys and Compounds, 2021, 855(2): 157485.

[13] WANG Fa-xing, WU Xiong-wei, LI Chun-yang, ZHU Yu-song, FU Li-jun, WU Yu-ping, LIU Xiang. Nanostructured positive electrode materials for post-lithium ion batteries [J]. Energy & Environmental Science, 2016, 9: 3570−3611.

[14] SHIN J W, SON J T. Novel core-shell-type design of $Na_{0.5}[Li_{0.5}(Ni_{0.8}Co_{0.1}Mn_{0.1})_{1-x}(Ni_{0.5}Co_{0.1}Mn_{0.4})_x]O_2$ cathode material for sodium-ion batteries [J]. Journal of Nanoscience and Nanotechnology, 2019, 19(3): 1335−1339.

[15] WANG Peng-fei, YAO Hu-rong, LIU Xin-yu, ZHANG Jie-nan, GU Lin, YU Xi-qian, YIN Ya-xia, GUO Yu-guo. Ti-substituted $NaNi_{0.5}Mn_{0.5-x}Ti_xO_2$ cathodes with reversible O3−P3 phase transition for high-performance sodium-ion batteries [J]. Advanced Materials, 2017, 29(19): 1700210.

[16] LI Tao, LI Xin-hai, WANG Zhi-xing, GUO Hua-jun. A short process for the efficient utilization of transition-metal chlorides in lithium-ion batteries: A case of $Ni_{0.8}Co_{0.1}Mn_{0.1}O_{1.1}$ and $LiNi_{0.8}Co_{0.1}Mn_{0.1}O_2$ [J]. Journal of Power Sources, 2017, 342: 495−503.

[17] MO Wen-bin, WANG Zhi-xing, WANG Jie-xi, LI Xin-hai, YAN Guo-chun. Tuning the surface of $LiNi_{0.8}Co_{0.1}Mn_{0.1}O_2$ primary particle with lithium boron oxide toward stable cycling [J]. Chemical Engineering Journal, 2020, 400(15): 125820.

[18] DAI Zheng-fei, ULAGANATHAN M, TAN Hui-teng, YAN Qing-yu. Advanced cathode materials for sodium-ion batteries: What determines our choices? [J]. Small Methods, 2017, 1(5): 1700098.

[19] YAN Guo-chun, MARIYAPPAN S, ROUSSE G, JACQUET Q, DESCHAMPS M, DAVID R, MIRVAUX B, FREELAND J W, TARASCON J M. Higher energy and safer sodium ion batteries via an electrochemically made disordered $Na_3V_2(PO_4)_2F_3$ material [J]. Nature Communications, 2019, 10(1): 585.

[20] KUBOTA K, KOMABA S. Review—Practical issues and future perspective for Na-ion batteries [J]. Journal of the Electrochemical Society, 2015, 162(14): A2538−A2550.

[21] WANG Peng-fei, YOU Ya. Layered oxide cathodes for sodium-ion batteries: Phase transition, air stability, and performance [J]. Advanced Energy Materials, 2018, 8(8): 1701912.

[22] PU Xiang-jun, WANG Hui-ming, ZHAO Dong, YANG Han-xi, AI Xin-ping, CAO Shu-nan, CHEN Zhong-xue, CAO Yu-liang. Recent progress in rechargeable sodium-ion batteries: Toward high−power applications [J]. Small, 2019, 15(32): 1805427.

[23] DELMAS C, FOUASSIER C, HAGENMULLER P. Structural classification and properties of the layered oxides [J]. Physica B+C, 1980, 99(1): 81−85.

[24] MOLENDA J, STOKLOSA A. Electronic and electro-chemical properties of nickel bronze, Na_xNiO_2 [J]. Solid State Ionics, 1990, 38(1/2): 1−4.

[25] BERTHELOT R, CARLIER D, DELMAS C. Electrochemical investigation of the P2-Na_xCoO_2 phase diagram [J]. Nature Materials, 2011, 10(1): 74−80.
[26] YANAGITA A, SHIBATA T, KOBAYASHI W, MORITOMO Y. Scaling relation between renormalized discharge rate and capacity in Na_xCoO_2 films [J]. APL Materials, 2015, 3(10): 1−8.
[27] BILLAUD J, CLEMENT R J, ARMSTRONG A R, CANALES-VÁZQUEZ J, ROZIER P, GREY C P, BRUCE P G. β-$NaMnO_2$: A high-performance cathode for sodium-ion batteries [J]. Journal of the American Chemical Society, 2014, 46(14): 17243−17248.
[28] KUMAKURA S, TAHARA Y, KUBOTA K, CHIHARA K, KOMABA S. Sodium and manganese stoichiometry of P2-type $Na_{2/3}MnO_2$ [J]. Angewandte Chemie, 2016, 128(41): 12952−12955.
[29] WU Yu-ping, WANG Fa-xing, WANG Xiao-wei, CHANG Zheng, ZHU Yu-song, FU Li-jun, LIU Xiang. Electrode materials with tailored facets for electrochemical energy storage [J]. Nanoscale Horizons, 2016, 1(4): 272−289.
[30] ZHAO Jie, ZHAO Li-wei, DIMOV N, OKADA S, NISHIDA T. Electrochemical and thermal properties of α-$NaFeO_2$ cathode for Na-ion batteries [J]. Journal of Power Sources, 2013, 244(5): 752−757.
[31] YABUUCHI N, YOSHIDA H, KOMABA S. Crystal structures and electrode performance of alpha-$NaFeO_2$ for rechargeable sodium batteries [J]. Electrochemistry, 2012, 80(10): 716−719.
[32] XIA Xin, DAHN J R. $NaCrO_2$ is a fundamentally safe positive electrode material for sodium-ion batteries with liquid electrolytes [J]. Electrochemical and Solid-State Letters, 2012, 15(1): A1−A4.
[33] DUFFORT V, TALAIE E, BLACK R, NAZAR L F. Uptake of CO_2 in layered P2-$Na_{0.67}Mn_{0.5}Fe_{0.5}O_2$: Insertion of carbonate anions [J]. Chemistry of Materials, 2015, 27(7): 2515−2524.
[34] LI Hui, LIU Shuang-yu, WANG Hui-ming, WANG Bo, CHEN Zhong-xue. Improved sodium storage performance of $Na_{0.44}MnO_2$ cathode at a high temperature by Al_2O_3 coating [J]. Acta Physico-Chimica Sinca, 2019, 35(12): 1357−1364.
[35] LI Yun-ming, YANG Zhen-zhong, XU Shu-yin, MU Lin-qin, GU Lin, HU Yong-sheng, LI Hong, CHEN Li-quan. Air-stable copper-based P2-$Na_{7/9}Cu_{2/9}Fe_{1/9}Mn_{2/3}O_2$ as a new positive electrode material for sodium-ion batteries [J]. Advanced Science, 2015, 2(6): 1500031.
[36] YAO Hu-rong, WANG Peng-fei, GONG Yue, ZHANG Jie-nan, YU Xi-qian, GU Lin, OUYANG Chu-ying, YIN Ya-xin, HU En-yuan, YANG Xiao-qing, STAVITSKI E, GUO Yu-guo, WAN Li-jun. Designing air-stable O3-type cathode materials by combined structure modulation for Na-ion batteries [J]. Journal of the American Chemical Society, 2017, 139(25): 8440−8443.
[37] ZHENG Li-tuo, LI Ling-jun, SHUNMUGASUNDARAM R, OBROVAC M N. Effect of controlled-atmosphere storage and ethanol rinsing on $NaNi_{0.5}Mn_{0.5}O_2$ for sodium-ion batteries [J]. ACS Applied Materials & Interfaces, 2018, 10(44): 38246−38254.

Al_2O_3 包覆改善 P2 型 $Na_{2/3}Fe_{1/2}Mn_{1/2}O_2$ 正极材料的存储性能

常轶娇，谢光辉，周雍茂，王接喜，王志兴，郭华军，尤编政，颜果春

中南大学 冶金与环境学院，长沙 410083

摘　要：采用超声喷雾热解与高温固相烧结相结合的方法合成 P2 型 $Na_{2/3}Fe_{1/2}Mn_{1/2}O_2$ 材料。通过 X 射线衍射仪、扫描电子显微镜和电化学充放电设备对材料的结构、形貌和电化学性能进行全面的表征。此外，在 $Na_{2/3}Fe_{1/2}Mn_{1/2}O_2$ 表面包覆 Al_2O_3 薄层，该包覆层可以抑制 $Na_2CO_3·H_2O$ 的形成，提高 $Na_{2/3}Fe_{1/2}Mn_{1/2}O_2$ 材料的存储性能，从而改善其电化学性能。这种简单的表面改性方法为合成高性能钠离子电池正极材料提供了新思路。

关键词：Al_2O_3 包覆；空气稳定性；喷雾热解；钠离子电池；铁锰氧化物

(Edited by Wei-ping CHEN)